Monthly Notices of the ROYAL ASTRONOMICAL SOCIETY

MNRAS **451,** 849–858 (2015) doi:10.1093/mnras/stv991

The Atacama Cosmology Telescope: measuring radio galaxy bias through cross-correlation with lensing

Rupert Allison,[1★] Sam N. Lindsay,[1] Blake D. Sherwin,[2] Francesco de Bernardis,[3] J. Richard Bond,[4] Erminia Calabrese,[1] Mark J. Devlin,[5] Joanna Dunkley,[1] Patricio Gallardo,[3] Shawn Henderson,[3] Adam D. Hincks,[6] Renée Hlozek,[7] Matt Jarvis,[1,8] Arthur Kosowsky,[9] Thibaut Louis,[1] Mathew Madhavacheril,[10] Jeff McMahon,[11] Kavilan Moodley,[12] Sigurd Naess,[1] Laura Newburgh,[13] Michael D. Niemack,[3] Lyman A. Page,[14] Bruce Partridge,[15] Neelima Sehgal,[10] David N. Spergel,[7] Suzanne T. Staggs,[14] Alexander van Engelen[4] and Edward J. Wollack[16]

[1]*Sub-department of Astrophysics, University of Oxford, Denys Wilkinson Building, Oxford OX1 3RH, UK*
[2]*Berkeley Center for Cosmological Physics, LBL and Department of Physics, University of California, Berkeley, CA 94720, USA*
[3]*Department of Physics, Cornell University, Ithaca, NY 14853, USA*
[4]*Canadian Institute for Theoretical Astrophysics, University of Toronto, Toronto, ON M5S 3H8, Canada*
[5]*Department of Physics and Astronomy, University of Pennsylvania, 209 South 33rd Street, Philadelphia, PA 19104, USA*
[6]*Department of Physics and Astronomy, University of British Columbia, Vancouver, BC V6T 1Z4, Canada*
[7]*Department of Astrophysical Sciences, Peyton Hall, Princeton University, Princeton, NJ 08544, USA*
[8]*Physics Department, University of the Western Cape, Bellville 7535, South Africa*
[9]*Department of Physics and Astronomy, University of Pittsburgh, Pittsburgh, PA 15260, USA*
[10]*Physics and Astronomy Department, Stony Brook University, Stony Brook, NY 11794, USA*
[11]*Department of Physics, University of Michigan, Ann Arbor, MI 48103, USA*
[12]*Astrophysics and Cosmology Research Unit, School of Mathematics, Statistics and Computer Science, University of KwaZulu-Natal, Durban 4041, South Africa*
[13]*Dunlap Institute for Astronomy and Astrophysics, University of Toronto, 50 St. George St., Toronto, ON M5S 3H4, Canada*
[14]*Joseph Henry Laboratories of Physics, Jadwin Hall, Princeton University, Princeton, NJ 08544, USA*
[15]*Department of Physics and Astronomy, Haverford College, Haverford, PA 19041, USA*
[16]*NASA/Goddard Space Flight Center, Greenbelt, MD 20771, USA*

Accepted 2015 May 1. Received 2015 April 28; in original form 2015 February 23

ABSTRACT

We correlate the positions of radio galaxies in the FIRST survey with the cosmic microwave background lensing convergence estimated from the Atacama Cosmology Telescope over 470 deg^2 to determine the bias of these galaxies. We remove optically cross-matched sources below redshift $z = 0.2$ to preferentially select active galactic nuclei (AGN). We measure the angular cross-power spectrum $C_l^{\kappa g}$ at 4.4σ significance in the multipole range $100 < l < 3000$, corresponding to physical scales within ≈2–60 Mpc at an effective redshift $z_{\rm eff} = 1.5$. Modelling the AGN population with a redshift-dependent bias, the cross-spectrum is well fitted by the *Planck* best-fitting Λ cold dark matter cosmological model. Fixing the cosmology and assumed redshift distribution of sources, we fit for the overall bias model normalization, finding $b(z_{\rm eff}) = 3.5 \pm 0.8$ for the full galaxy sample and $b(z_{\rm eff}) = 4.0 \pm 1.1 (3.0 \pm 1.1)$ for sources brighter (fainter) than 2.5 mJy. This measurement characterizes the typical halo mass of radio-loud AGN: we find $\log(M_{\rm halo}/{\rm M}_\odot) = 13.6^{+0.3}_{-0.4}$.

Key words: large-scale structure of Universe – radio continuum: galaxies.

1 INTRODUCTION

Radio galaxies trace the large-scale structure in the Universe which has been measured with large-area surveys including FIRST, WENSS, NVSS and SUMSS (Becker, White & Helfand 1995;

★ E-mail: rupert.allison@astro.ox.ac.uk

© 2015 The Authors
Published by Oxford University Press on behalf of the Royal Astronomical Society

Downloaded from http://mnras.oxfordjournals.org/ at NASA Goddard Space Flight Ctr on November 16, 2015

Rengelink et al. 1997; Condon et al. 1998; Bock, Large & Sadler 1999); for an overview see de Zotti et al. (2010). The angular clustering of these galaxies has been measured by Cress et al. (1996), Magliocchetti et al. (1998), Blake & Wall (2002), Overzier et al. (2003), Blake, Mauch & Sadler (2004b) and Lindsay et al. (2014a). The clustering of radio galaxies will soon be measured over much larger volumes of the Universe with the Square Kilometre Array (SKA) and its precursors, allowing cosmological effects such as dark energy, modified gravity and non-Gaussianity to be probed (e.g. Blake et al. 2004a; Carilli & Rawlings 2004; Camera et al. 2012; Raccanelli et al. 2012; Maartens et al. 2013, 2015; Norris et al. 2013; Abdalla et al. 2015; Jarvis et al. 2015; Santos et al. 2015).

The bias b of a large-scale structure tracer relates overdensities of that tracer δ to overdensities of the underlying dark matter field $\delta_{\rm DM}$:

$$\delta = b\delta_{\rm DM}. \quad (1)$$

Radio-selected galaxies broadly contain two populations: high-redshift active galactic nuclei (AGN) and low-redshift star-forming galaxies (SFGs; Condon, Cotton & Broderick 2002). AGN dominate the radio emission at high flux ($\gtrsim$ 1 mJy) and are highly biased, their hosts being among the most massive galaxies in the early Universe (e.g. Jarvis et al. 2001a; Rocca-Volmerange et al. 2004; Seymour et al. 2007; de Zotti et al. 2010; Fernandes et al. 2015). Their bias depends strongly on galaxy mass and redshift (e.g. Seljak & Warren 2004), and is poorly constrained particularly at high redshift where few optical counterparts are observed. Some progress has been made by identifying redshifts spectroscopically: using Galaxy And Mass Assembly (GAMA) data the bias of FIRST radio galaxies was measured at $z \approx 0.34$ over 200 deg^2 to the 10 per cent level (Lindsay et al. 2014a). On a smaller square degree region, clustering measurements using data from the Very Large Array (VLA) and VISTA Deep Extragalactic Observations (Jarvis et al. 2013) were used to show evidence for a strongly increasing bias at $z > 2$ (Lindsay, Jarvis & McAlpine 2014b).

An alternative way to constrain bias is through cross-correlation of the tracer fluctuations with gravitational lensing due to large-scale structure. In particular, the lensing of the cosmic microwave background (CMB) measures the integrated matter fluctuations to $z \approx 1100$. As we will show the high-redshift radio source distribution overlaps strongly with the broad CMB lensing kernel. Cross-correlations between the CMB and other tracers of large-scale structure have been reported by e.g. Smith, Zahn & Doré (2007), Hirata et al. (2008), Feng et al. (2012), Bleem et al. (2012), Planck Collaboration XVIII (2014c), van Engelen et al. (2014), Fornengo et al. (2015) and Bianchini et al. (2015). Planck Collaboration XVII (2014b) detect the correlation of lensing with radio galaxies from NVSS at 20σ. Sherwin et al. (2012) correlate lensing measurements from the Atacama Cosmology Telescope (ACT) with optically selected quasars from the Sloan Digital Sky Survey (SDSS), measuring a bias of $b = 2.5 \pm 0.6$ at an effective redshift $z \approx 1.4$. Geach et al. (2013) correlate lensing from the South Pole Telescope (SPT) with quasars selected from the *Wide-field Infrared Survey Explorer* (*WISE*), measuring a bias $b = 1.61 \pm 0.22$ at $z \approx 1.0$. An advantage of cross-correlations is that they are robust to systematic biases which may be particular to each data set.

In this paper, we measure the angular cross-power spectrum $C_l^{\kappa g}$ between the lensing convergence estimated from ACT with the FIRST radio source overdensity. We use lensing maps from the 3-year ACT Equatorial survey (Das et al. 2014) together with the first-season ACTPol survey (Madhavacheril et al. 2015; Naess et al. 2014; van Engelen et al. 2014). We consider 36 000 radio sources with flux brighter than 1 mJy, and remove optically cross-matched sources from the SDSS (York et al. 2000) at $z < 0.2$ to preferentially select AGN, discarding the majority of low-redshift SFGs. We use this to estimate the bias normalization, assuming a fixed cosmological model, and using a redshift distribution and bias-evolution model from the simulated radio catalogue of the SKA Design Study (SKADS; Wilman et al. 2008). We measure $C_l^{\kappa g}$ across a wide range of scales ($100 < l < 3000$) and consider various splits of the radio sources to investigate redshift and flux dependence of the bias.

We describe the lensing and radio data and the cross-correlation analysis methods in Section 2. The results and discussion are presented in Section 3, with further interpretation of the AGN bias in Section 3.1. We conclude in Section 4.

2 DATA AND ANALYSIS

2.1 ACT and ACTPol

The ACT is located at an altitude of 5190 m in Parque Astronómico Atacama in Northern Chile. The telescope and its current polarization-sensitive receiver, ACTPol, are described in Niemack et al. (2010). The two seasons of ACT temperature data and the ACTPol first-season temperature and polarization data used in this analysis are presented in Das et al. (2013) and Naess et al. (2014). Lensing by large-scale structure induces coupling of otherwise independent temperature and polarization modes. We construct estimators of the lensing convergence from quadratic combinations of temperature and polarization maps in Fourier space, following the methodology of Hu & Okamoto (2002). We use the same lensing convergence maps and Monte Carlo simulations as described by Das et al. (2011) and van Engelen et al. (2014).

In this analysis, we use two ACT data sets. The first is the ACT Equatorial data which span a thin strip along the celestial equator with an area of 300 deg^2. This strip is partitioned into six approximately equal-area patches over which we compute the cross-spectrum separately and then average (weighting by patch area) for the final result. We lose negligible information at the scales of interest and it allows for patch-to-patch consistency checks. The effective white-noise component of the two-season co-added data is 18 μK arcmin.

We also fold in the three ACTPol 'deep' fields from the first-season data set, labelled D1, D5 and D6, with a temperature white-noise component of 16.2, 13.2, 11.2 μK arcmin, respectively, over a total area of 206 deg^2 (37 deg^2 of which overlaps with the ACT Equatorial strip). All maps in this analysis use 0.5 arcmin × 0.5 arcmin pixels, and their positions are shown in Fig. 1.

For each ACTPol patch, we use the minimum-variance (MV) linear combination of the reconstructed convergence maps estimated from each quadratic pair (TT, TE, EE, EB). Following Ade P. A. R. et al. (POLARBEAR Collaboration 2014), van Engelen et al. (2014) and Story et al. (2014), we perform the combination in Fourier space, weighting each convergence map by the mode-dependent inverse-variance noise to obtain the MV combination. All lensing convergence maps are mean-field subtracted to remove the lensing-like effect at large scales of mode-coupling from the windowing of the temperature and polarization fields.

As described in van Engelen et al. (2014), an apodization window is applied to the ACT and ACTPol temperature and polarization map prior to lensing reconstruction. This windowing operation includes

Downloaded from http://mnras.oxfordjournals.org/ at NASA Goddard Space Flight Ctr on November 16, 2015

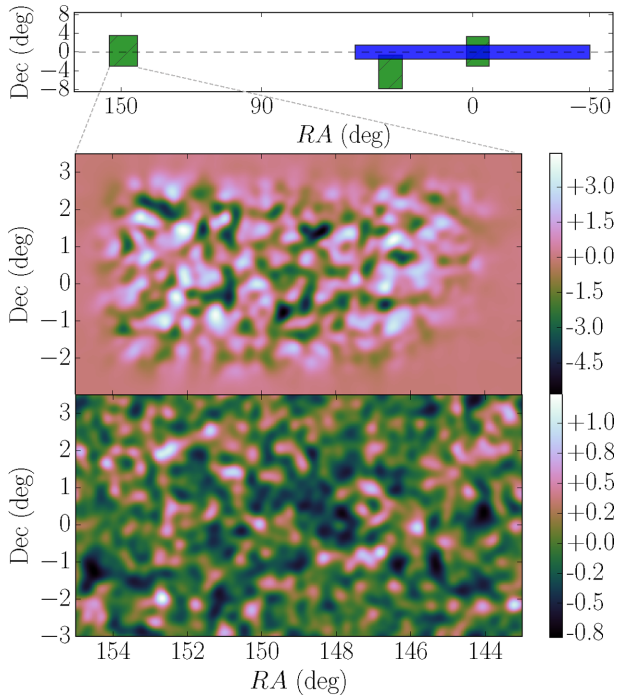

Figure 1. Top panel: footprint of the patches used in this analysis: ACT (blue, filled) and ACTPol (green, hatched, left to right: D1, D6, D5). Middle panel: ACTPol D1 lensing convergence map κ smoothed to suppress power below 20 arcmin scales. The spatial modulation, primarily due to the windowing of the temperature and polarization maps by the pixel weight map, is evident. The ACTPol lensing convergence is noise dominated for scales $\lesssim 1$ deg. Bottom panel: the FIRST overdensity field g over the same patch, smoothed to the same scale, is noise dominated at all scales.

a cosine taper at the map edges to remove discontinuous edges and weighting by the pixel hitmap to optimize the signal-to-noise of the reconstruction. The resulting quadratic estimator reconstruction is therefore also windowed, resulting in a scale-dependent suppression of power. Following Bleem et al. (2012), Sherwin et al. (2012), van Engelen et al. (2014) and Hand et al. (2015), we use realistic Monte Carlo simulations to calculate the transfer function correction by computing the mean cross-spectrum between noiseless lensing realizations and their corresponding reconstructions within the lensing pipeline. This correction (<5 per cent for ACTPol, ≈10 per cent for ACT) is then applied to the maps when computing the data cross-spectrum to account for the suppression of power due to windowing.

2.2 FIRST

The FIRST survey (Becker et al. 1995) was carried out between 1993 and 2011 at 1.4 GHz with the VLA in B configuration. The final catalogue (Helfand, White & Becker 2015) contains 946 432 sources covering 10 575 deg^2, with an angular resolution of 5.4 arcsec (full width at half-maximum, FWHM) and to a completeness of 95 per cent at flux $S_{1.4\,\mathrm{GHz}} > 2$ mJy. The oblique decision-tree program developed by the FIRST survey team (White et al. 1997) determines the probability that each catalogue entry is the result of a spurious sidelobe response to a nearby bright source. We exclude entries with a sidelobe probability of >0.1, leaving 720 219 sources above 1 mJy.

To address the issue of extended radio sources resulting in multiple detections for one host galaxy, perhaps none of which corresponds to the core itself (and therefore any associated optical source), we have followed Cress et al. (1996) in applying a collapsing radius of 72 arcsec (0.02 deg) to the FIRST catalogue. Any FIRST sources within this radius of one another are grouped and combined to form a single entry, positioned at the flux-weighted average coordinates of the group, and attributed with their total flux density. Around 32 per cent of all FIRST sources are collapsed (in groups of average size 2.3 sources per group), forming 17 per cent of the resulting catalogue. These multiple-component sources will come from AGN, which dominate the source population at high flux density and high redshift; at lower flux density and redshift, starbursts and normal SFGs are increasingly dominant (Condon et al. 2002).

The redshifts of individual sources are not determined by FIRST, but can be found by identifying counterparts in SDSS, which gives redshifts for the brighter, nearby sources in the FIRST sample. The closest sources are most likely SFGs (e.g. Condon et al. 2002; Wilman et al. 2008); by removing them we simplify the measurement as a constraint on the bias of the dominant astrophysical population (i.e. AGN).

We do this by initially taking all sources in the catalogue which lie in the ACT and ACTPol patches described above (≈38 000 sources). AGN dominate the radio luminosity function for $L_{1.4\,\mathrm{GHz}} > 10^{23}$ W Hz^{-1} (Condon et al. 2002; Jarvis & Rawlings 2004; Mauch & Sadler 2007). Given the flux limit of FIRST (1 mJy), and assuming a spectral index of $\alpha = 0.8$ ($S_\nu \propto \nu^{-\alpha}$) for the AGN, this luminosity threshold corresponds to sources above redshift $z = 0.2$. We identify optical matches to the radio sources within SDSS, treating as reliable all matches within 2 arcsec of the radio source following Lindsay et al. (2014a). Given the density of SDSS sources, the level of spurious optical matches identified with this technique is below 2 per cent. A fraction of 0.27 of the FIRST sources in the lensing fields have an optical match obtained in this manner. We remove all sources with a known redshift below $z = 0.2$, constituting 18 per cent of the sources with a reliable redshift, or 5 per cent of the total number of sources. Given the small fraction of sources removed, this procedure has only a small effect on the results (Section 3). The final sample comprises ≈36 000 sources with a mean angular density of 71 sources deg^{-2}.

Within each ACT and ACTPol patch, a corresponding map of the overdensity of sources g is produced in a similar way to Sherwin et al. (2012) and Geach et al. (2013). We create a map at the same pixelation as the lensing map and define the radio galaxy overdensity map g by

$$g_i = \frac{n_i}{\bar{n}} - 1, \tag{2}$$

where n_i is the number of sources in each pixel and $\bar{n}$ is the mean number of galaxies per pixel. This overdensity map is then smoothed with a Gaussian with FWHM of 2 arcmin to obtain a well-defined pixel window function.

2.3 Analysis methods

We compute the cross-spectrum between the lensing convergence from ACT and ACTPol with the FIRST radio galaxy overdensity.

Following the procedures outlined in Das et al. (2011) and Hand et al. (2015), we correct for mode-coupling induced by windowing in real space and from applying annular binning in Fourier space, computing an unbiased estimator of the binned cross-spectrum $C_b^{\kappa g}$. The binning we adopt is given in Table 1.

To determine the full band-power covariance matrix, we cross-correlate realistic simulations of the reconstructed lensing fields with the radio source maps (which are in principle uncorrelated).

Downloaded from http://mnras.oxfordjournals.org/ at NASA Goddard Space Flight Ctr on November 16, 2015

Table 1. The measured cross-spectrum $C^{\kappa g}_{b,\mathrm{ACT}}$ for FIRST radio sources with ACT and ACTPol lensing. The bins are chosen to be wide enough that correlations are small (<10 per cent, Section 2.3), but narrow enough to resolve structure in the cross-spectrum.

Bin b	[$l_{\min}$, $l_{\max}$]	$C^{\kappa g}_{b,\mathrm{ACT}}$ ($\times 10^7$)	$C^{\kappa g}_{b,\mathrm{ACTPol}}$ ($\times 10^7$)	$C^{\kappa g}_{b,\mathrm{comb}}$ ($\times 10^7$)
200	[100,300]	1.76 ± 0.74	2.04 ± 0.80	1.89 ± 0.54
450	[301,600]	0.59 ± 0.32	-0.20 ± 0.42	0.30 ± 0.25
750	[601,900]	0.57 ± 0.25	0.32 ± 0.31	0.48 ± 0.19
1050	[901,1200]	0.28 ± 0.20	0.38 ± 0.26	0.32 ± 0.16
1350	[1201,1500]	0.17 ± 0.16	-0.08 ± 0.22	0.09 ± 0.13
1650	[1501,1800]	0.04 ± 0.15	0.01 ± 0.19	0.03 ± 0.12
1950	[1801,2100]	0.11 ± 0.14	-0.00 ± 0.18	0.07 ± 0.11
2250	[2101,2400]	0.07 ± 0.14	-0.01 ± 0.17	0.04 ± 0.11
2550	[2401,2700]	0.06 ± 0.14	0.19 ± 0.18	0.11 ± 0.11
2850	[2701,2999]	-0.01 ± 0.13	-0.23 ± 0.19	-0.08 ± 0.11

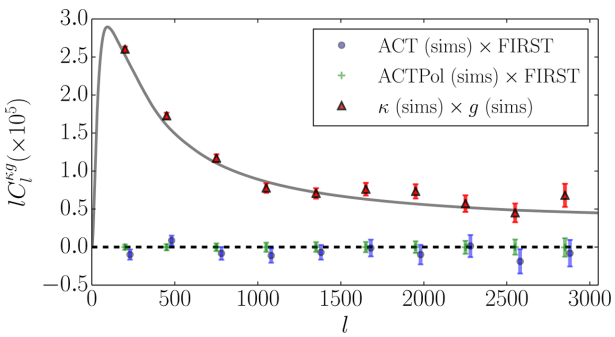

Figure 2. Pipeline validation: mean cross-spectrum $lC_l^{\kappa g}$ of the FIRST radio source map with ACTPol lensing simulations (green dashes, $N_{\mathrm{sims}} = 2048$) and ACT lensing simulations (blue circles, $N_{\mathrm{sims}} = 480$) as described in Section 2.3. We displace the ACT points by $\Delta l = 30$ to the right for visual clarity. The measurements are consistent with null, demonstrating that our pipeline does not induce spurious cross-power in the absence of correlation. Error bars shown are the diagonal components of the empirical covariance matrix derived from the same Monte Carlo simulations, scaled appropriately by $\sqrt{N_{\mathrm{sims}}}$. We also show the recovered mean cross-spectrum from realistic *correlated* simulations (red triangles, Section 2.3). We cross-correlate input convergence maps, which have added scale-dependent Gaussian noise, with correlated realizations of a galaxy field. This demonstrates that our pipeline is able to recover in an unbiased fashion a known input cross-spectrum [although we note that this does not test the lensing reconstruction pipeline, for which we refer to the systematic tests in van Engelen et al. (2014)]. The generative model for the cross-spectrum is not the fiducial cross-spectrum, but this is unimportant for the purposes of this test.

Production of these realistic simulations is described in Das et al. (2011) and van Engelen et al. (2014).

This procedure ignores the cosmic variance contribution to the uncertainties in the data coming from the correlated part of the two maps, $C_l^{\kappa g}$. We neglect this as both maps are noise dominated at the relevant scales for this analysis. Bin-to-bin correlations are <10 per cent for all off-diagonal elements of the covariance matrix. We also check that the mean cross-spectrum is consistent with null (Fig. 2), confirming that our pipeline does not induce spurious cross-power in the absence of correlation.

Approximately 50 per cent of the ACTPol D5 patch and 15 per cent of D6 overlap with the ACT Equatorial strip (Fig. 1). There is therefore a correlation between the ACT and ACTPol cross-spectra, as common CMB modes in the primary temperature map have been used to reconstruct the lensing convergence over these regions. Noiseless temperature maps from ACT and ACTPol, and negligible polarization information from ACTPol, would result in a perfect correlation between the reconstructed convergence maps. However, this overlapping area represents 37 deg^2 of the total 470 deg^2 of this analysis, and hence at most a 4 per cent overestimate of the detection significance, which we neglect given the statistical errors. We thus average the ACT and ACTPol data cross-spectra with inverse-variance weighting.

In order to check for bias in the cross-spectrum estimator, we ran 500 pairs of simple simulated convergence and radio density maps through the cross-correlation pipeline, generating new *correlated* simulations. To obtain these pairs, we draw as signal maps aperiodic correlated Gaussian realizations from power spectra obtained assuming *Planck* best-fitting cosmological parameters and a fiducial bias model and source distribution for the radio galaxies (Kamionkowski, Kosowsky & Stebbins 1997; Planck Collaboration XVI 2014a). We add Gaussian noise realizations to the convergence maps, appropriate for the temperature sensitivity of ACT (Section 2.1), using the formalism of Hu & Okamoto (2002) to calculate the reconstruction noise. ACTPol maps are less noisy, but the precise noise level is unimportant for this test. For each pixel i in the radio signal map g, we draw a Poisson random variable X_i with mean $\bar{n}(1 + g_i)$, where $\bar{n}$ is the average number of sources per pixel. We set $\bar{n} = 71$ sources deg^{-2} to reflect the source density in the data. We then redefine $g_i \leftarrow X_i/\bar{n} - 1$ and finally smooth the resulting map with a Gaussian beam of FWHM 2 arcmin.

These simulated maps, by construction, have signal, noise and correlation properties which mimic the data, although they do not have the full spatially anisotropic noise properties. These lensing simulations have not been processed through the lensing reconstruction pipeline, but here we use them simply for checking bias in the cross-correlation pipeline. We refer to the systematic tests in van Engelen et al. (2014) for checks of the lensing pipeline. We find that we do not require apodization of the maps to produce the observed unbiased results; the mean auto- and cross-spectra of these simulations are consistent with the assumed input spectra (Fig. 2).

2.4 Modelling

The theoretical cross-spectrum can be written under the Limber approximation as

$$C_l^{\kappa g} = \int_0^\infty \mathrm{d}z \frac{H(z)}{\chi^2(z)} W_\kappa(z) W_g(z) P\left(\frac{l}{\chi(z)}, z\right), \tag{3}$$

where $H(z)$ is the Hubble parameter, $\chi(z)$ is the comoving distance to redshift z, $P(k, z)$ is the non-linear matter power spectrum (wavenumber $k = l/\chi$) and $\{W_i\}$ are the appropriate kernels for the two dark matter probes κ, g which are plotted in Fig. 3. The dominant term in W_g is directly proportional to the tracer bias $b(z)$ multiplied by the normalized source redshift distribution $\mathrm{d}n/\mathrm{d}z$:

$$W_g(z) = b(z)\frac{\mathrm{d}n}{\mathrm{d}z} + M(z), \tag{4}$$

where $M(z)$ is a sub-dominant contribution from the magnification bias. The magnification bias term is independent of the tracer bias, and the full expression (given in e.g. Sherwin et al. 2012) is calculated directly, using the fiducial redshift distribution of FIRST sources in our sample and the inferred slope ($s \approx 0.3$) at the faint end of the luminosity function from the SKADS radio catalogue (see below). The magnification bias contributes a small (<6 per cent), negative contribution to the total cross-spectrum across all relevant scales, and we include it throughout for modelling of the

Downloaded from http://mnras.oxfordjournals.org/ at NASA Goddard Space Flight Ctr on November 16, 2015

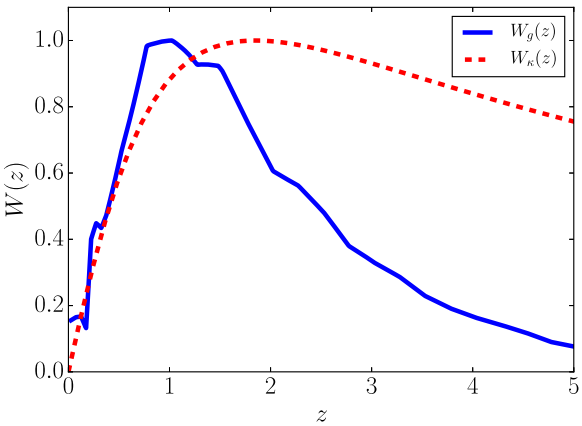

Figure 3. Cross-spectrum kernels for the radio sources (g) and CMB lensing (κ), normalized to a unit maximum; see equation (3). The extensive overlap between the kernels implies a large correlation coefficient between the two fields.

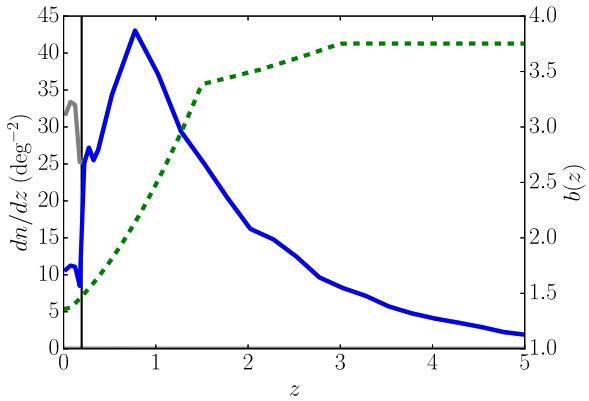

Figure 4. Green dashed: fiducial bias model $b(z)$, constructed as a weighted average of the constituent source population bias models (Section 2.2). Blue solid: source redshift distribution model as derived from SKADS and including the cut of a fraction of the $z < 0.2$ sources.Vertical black line: $z = 0.2$. Grey solid: as previous but without the redshift cut.

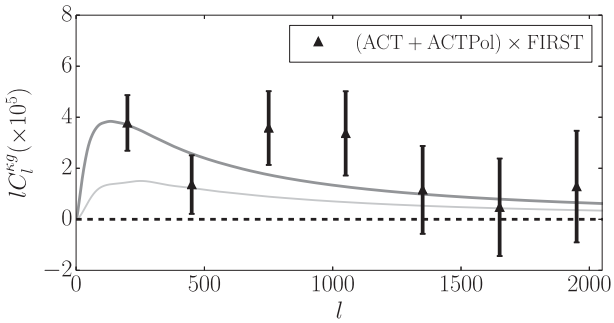

Figure 5. Data cross-spectrum $lC_l^{\kappa g}$ for (ACT+ACTPol) × FIRST. Dark grey, solid: the best-fitting cross-spectrum. Light grey, solid: the contribution from $z > 1.5$ sources. We restrict the plot to $l < 2000$ where the signal-to-noise dominates. We show as error bars the diagonal components of the empirical covariance matrix derived from Monte Carlo simulations (Section 2.3). Scaling the amplitude of the fiducial bias model, the combined significance of the bias detection is 4.5σ (Section 3).

cross-spectrum. A rescaling of the bias amplitude therefore corresponds linearly to a rescaling of the cross-spectrum $C_l^{\kappa g}$. We compute the theory $P(k, z)$ using best-fitting *Planck* cosmological parameters, including non-linear corrections using CAMB with Halofit (Lewis, Challinor & Lasenby 2000; Smith et al. 2003; Takahashi et al. 2012).

We use the SKADS simulated radio continuum catalogue to construct a fiducial bias model $b(z)$ and redshift distribution $\mathrm{d}n/\mathrm{d}z$ for the $S_{1.4\,\mathrm{GHz}} > 1$ mJy radio sources (see Wilman et al. 2008, 2010, for details). We neglect any scale dependence in the bias model; see Section 3 for further discussion. The simulation lacks the mass resolution to directly resolve galaxy- and group-sized haloes for a robust implementation of the galaxy clustering, but the source counts, redshift distribution and variations in space density are defined by extrapolating observed luminosity functions, and implementing a bias model, for each of five individual radio populations: AGN (FR I and FR II types, radio-quiet quasars), normal SFGs and starburst galaxies. These populations are assigned a single halo mass each, used to define $b(z)$ as described by Mo & White (1996), with the bias held fixed above a particular redshift to prevent unphysical clustering where the bias is poorly constrained observationally (see fig. 3 of Raccanelli et al. 2012). The simulated catalogue informs us how the relative numbers of these populations evolve with redshift, and how the observed bias will evolve accordingly for a mixed sample of sources.

Fixing the bias above a particular redshift for each population is clearly a crude model, and is necessitated by the (itself unphysical) assumption of a fixed halo mass for each population adopted in Wilman et al. (2008); this must break down at high redshifts. Little is known about the high-redshift bias of radio sources, and better-motivated models are lacking (Section 1). If the data in this study, and studies like this, strongly prefer a much higher bias at high redshift, this will be reflected in the inferred bias normalization or a poor model fit.

By comparing the distribution of known source redshifts (Section 2.2) with the SKADS simulation, we find that an estimated 66 per cent of low-redshift sources are removed by the $z < 0.2$ cut. To construct $\mathrm{d}n/\mathrm{d}z$, we therefore weight $z < 0.2$ sources by 0.34 relative to higher redshift sources, similar to the approach of Lindsay et al. (2014b). After the redshift cut, ≈96 per cent of the sources in our sample are expected to be AGN, with a ≈4 per cent contamination fraction of star-forming and starburst galaxies, and we estimate the final sample to have a median redshift $\tilde{z} = 1.3$. These fiducial models are shown in Fig. 4.

We emphasize that $C_l^{\kappa g}$ is a function of the product $b(z)\mathrm{d}n/\mathrm{d}z$, and so inference about the tracer bias is contingent on knowledge of the underlying redshift distribution. We discuss the limitations of assuming a fixed redshift distribution, and the effect of not removing the low-redshift sources, in Section 3.3.

Finally, we bin the theoretical cross-spectrum as for the data, accounting for the mode-coupling matrix of each patch (Das et al. 2011). We then compare the model to the data using a Gaussian likelihood, accounting for the full bin-to-bin covariance as derived from Monte Carlo simulations (Section 2.3). We primarily fit for an overall scaling A to the fiducial bias model, such that $b(z) \rightarrow Ab(z)$.

3 RESULTS

The cross-spectra for ACT × FIRST, ACTPol × FIRST and their combination are shown in Figs 5 and 6 and reported in Table 1. We find $A_{\mathrm{ACT}} = 1.22 \pm 0.31$ and $A_{\mathrm{ACTPol}} = 0.85 \pm 0.36$, with combined constraint $A = 1.06 \pm 0.24$. The goodness-of-fit statistics for these best-fitting models are reported in Table 2, and account for the small

Downloaded from http://mnras.oxfordjournals.org/ at NASA Goddard Space Flight Ctr on November 16, 2015

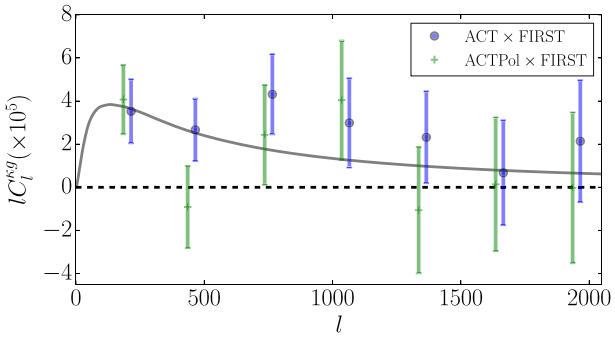

Figure 6. Data cross-spectrum $lC_l^{\kappa g}$ for ACT × FIRST (blue) and ACTPol × FIRST (green). Dark grey, solid: the best-fitting cross-spectrum for the combined data. Light grey, solid: the contribution from $z > 1.5$ sources. The ACT and ACTPol points have been displaced to the right and left by $\Delta l = 15$, respectively, for visual clarity. We show as error bars the diagonal components of the empirical covariance matrix derived from Monte Carlo simulations (Section 2.3).

Table 2. Results showing the bias amplitude A relative to the fiducial model of Fig. 4. We also quote the signal-to-noise ratio S/N, chi-squared values at the best-fitting χ^2, the number of degrees of freedom ν and the probability to exceed this χ^2 (PTE) under the assumption of the best-fitting model.

	A	S/N	χ^2 (ν)	PTE
ACT	1.22 ± 0.31	3.9	3.2 (9)	0.96
ACTPol	0.85 ± 0.36	2.4	7.2 (9)	0.62
Comb.	1.06 ± 0.24	4.5	11.0 (19)	0.92

(<10 per cent) bin-to-bin correlations (Section 2.3). This amplitude is consistent with the expected bias from the radio simulations; we interpret the result further in Section 3.1.

The parameter A only scales the bias-dependent part of the theoretical model. To assess the overall detection significance, we rescale the amplitude of the total theoretical cross-spectrum by a free parameter α: $C_l^{\kappa g} \rightarrow \alpha C_l^{\kappa g}$. This is equivalent to equally rescaling both terms in equation (4), including the magnification bias term. The combined data require $\alpha = 1.06 \pm 0.24$, and the cross-spectrum is detected at $\sqrt{\chi^2_{\rm null} - \chi^2_{\rm bf}} = 4.4\sigma$ statistical significance. Here $\chi^2_{\rm null} = 31.4$ is the chi-squared value of the fit under the null hypothesis (no cross-correlation) and $\chi^2_{\rm bf} = 11.0$ is the chi-squared value for the best-fitting model (number of degrees of freedom $\nu = 19$).

The mean cross-spectrum of ACT and ACTPol Monte Carlo simulations with the FIRST data set is shown in Fig. 2 and is consistent with null (Section 2.3). These simulations reproduce the amplitude and statistics of the lensing field but not the true mass distribution on the sky.

We further test our pipeline, checking for spurious correlations present only in the lensing and galaxy data, by performing two additional null tests.

First, we randomly permute the six FIRST patches within the equatorial strip, such that all patches are moved from their true position, with respect to the fixed ACT patches. We recompute the cross-spectrum, shown in Fig. 7. Fitting the normalization of the fiducial bias model A to these data, we obtain $A_{\rm ACT,\ shuffle} = -0.18 \pm 0.31$, consistent with null. The chi-squared value of the null hypothesis is 18.2 for $\nu = 10$ degrees of freedom, or a probability to exceed the observed chi-squared of 5 per cent.

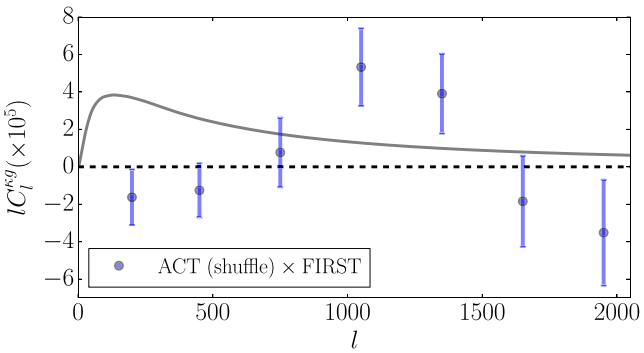

Figure 7. Cross-correlation between shuffled FIRST maps with ACT lensing convergence. Fitting the normalization of the fiducial bias model A to these data, we obtain $A_{\rm ACT,\ shuffle} = -0.18 \pm 0.31$, consistent with null (Section 3). Grey solid curve: cross-spectrum for the fiducial bias model which best fits the data of Fig. 5.

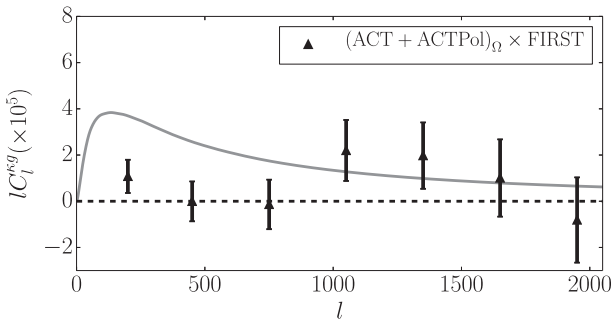

Figure 8. Cross-spectrum $lC_l^{\kappa g}$ between ACT+ACTPol lensing curl maps Ω and FIRST (Section 3). We restrict to $l < 2000$ for comparison with Fig. 5. Fitting the normalization of the fiducial bias model A to these data, we obtain $A_\Omega = 0.19 \pm 0.17$ and a chi-squared value of the null hypothesis of 21.8 for $\nu = 19$ degrees of freedom (a probability to exceed of 0.29). As expected this cross-correlation is consistent with null. Grey solid curve: cross-spectrum for the fiducial bias model which best fits the data of Fig. 5.

Secondly, we make reconstructions of the lensing field where the deflection field has been redefined – as the curl of the lensing potential – and hence the expected 'convergence' Ω is zero, following Sherwin et al. (2012) and van Engelen et al. (2014). These maps contain reconstruction noise but should contain no common signal with the overlapping galaxy field. We recompute the cross-spectrum of the lensing curl maps Ω with the FIRST maps, shown in Fig. 8. Fitting the normalization of the fiducial bias model A to these data, we obtain $A_\Omega = 0.19 \pm 0.17$. Error bars are calculated from the data auto-spectra using the Knox formula (Knox 1995). The chi-squared value of the null hypothesis is 21.8 for $\nu = 19$ degrees of freedom, or a probability to exceed of 0.29, confirming a null result.

Removal of the known $z < 0.2$ sources, which constitute ≈5 per cent of the FIRST sample (Section 2.2), has only a small effect on the inferred bias amplitude: without removal we find a combined constraint $A_{\rm noZcut} = 1.08 \pm 0.24$, consistent with expectations given the shape of the lensing kernel and low bias of SFGs at low redshift.

Restricting the analysis to multipoles $l < 900$, representing linear scales at the effective redshift $z_{\rm eff} = 1.5$, we find $A = 1.01 \pm 0.24$, giving a detection significance of 4.2σ. We conclude that any scale dependence of the bias on non-linear scales is unimportant for this measurement

Downloaded from http://mnras.oxfordjournals.org/ at NASA Goddard Space Flight Ctr on November 16, 2015

3.1 AGN bias

The primary results of this section are shown in Fig. 9. We determine the redshifts to which our measurement is most sensitive by considering the kernel $C_l^{\kappa g}(z) \equiv W_\kappa(z)W_g(z)P(l/\chi(z);z)$ of the theoretical cross-spectrum (equation 3; shown in Fig. 10). At $l = 200$, where the signal-to-noise of the cross-spectrum peaks, the mean redshift of the kernel is $\int zC_{200}^{\kappa g}(z)\mathrm{d}z/C_{200}^{\kappa g} = 1.5$. We adopt $z_{\rm eff} = 1.5$ as the effective redshift of the measurement, estimating $b(z_{\rm eff}) = 3.5 \pm 0.8$. We note however that we are sensitive to a range of redshifts: at $l = 200$ the kernel is non-negligible (>10 per cent of its peak value) out to redshifts $z > 3$, and the kernel shifts to higher redshifts at smaller scales. High-redshift sources make an important contribution to the small-scale cross-spectrum.

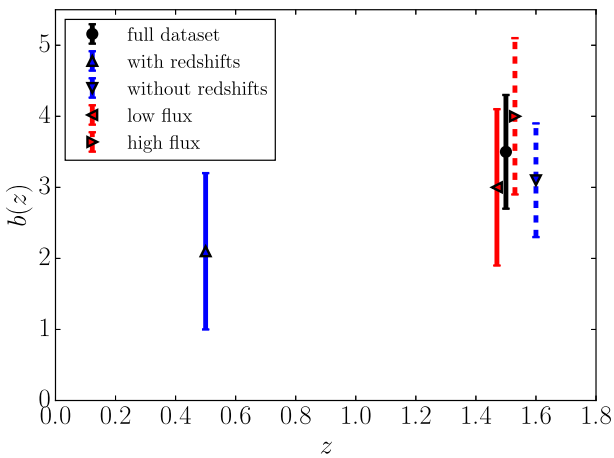

Figure 9. Summary of the primary bias results from Sections 3 and 3.1. For various data splits, we plot the corresponding constraint on the bias at the effective redshift $z_{\rm eff}$ of the measurement. We show the full data set constraint (black, solid, circle), the constraint for faint (red, solid, left triangle) and bright (red, dashed, right triangle) sources, and the constraint for sources with (blue, solid, upper triangle) and without (blue, dashed, lower triangle) individual identified redshifts. We displace the red points slightly (from $z_{\rm eff} = 1.5$) for visual clarity.

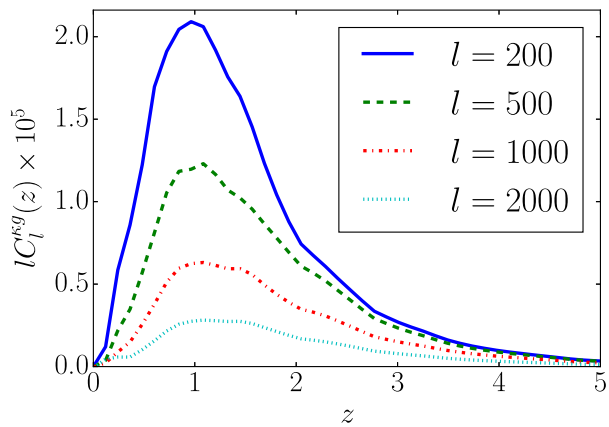

Figure 10. Cross-power spectrum kernel $C_l^{\kappa g}(z) \equiv W_\kappa(z)W_g(z)P(l/\chi(z);z)$, demonstrating the scale-dependent sensitivity of the cross-spectrum to source redshift. At $l = 200$, where the signal-to-noise peaks, the mean redshift of the kernel is $\int zC_{200}^{\kappa g}(z)\mathrm{d}z/C_{200}^{\kappa g} = 1.5$, which we adopt as the effective redshift $z_{\rm eff}$ of the radio source bias measurement. The spread in the kernel reflects sensitivity to a wide range of redshift. See Section 2.3 for details.

We consider a set of variations to the bias model. First, we fit the data with a redshift-independent bias model, varying the amplitude b. We find $b = 2.8 \pm 0.6$, with $\chi^2_{\rm bf} = 11.2$. Our data alone cannot distinguish a redshift-independent bias model from an evolving bias model, although our redshift-dependent model is more physically motivated by theoretical and empirical observations (e.g. Wilman et al. 2008; Lindsay et al. 2014b).

We probe the flux dependence of the AGN bias by splitting the FIRST sources into two roughly equal-sized subsamples, with a partition at 2.5 mJy. We create new maps of these FIRST sources, as described in Section 2.2. From SKADS, we estimate the normalized redshift distribution for each subsample, finding that they are equal to within ≈15 per cent across $0.3 < z < 4$, calculate $z_{\rm eff} = 1.5$ for both subsamples and estimate that the bias amplitude is ≈20 per cent higher in the bright sample. We repeat the analysis of Section 2.3, finding $b(z_{\rm eff}; F > 2.5\ \mathrm{mJy}) = 4.0 \pm 1.1$ and $b(z_{\rm eff}; F < 2.5\ \mathrm{mJy}) = 3.0 \pm 1.1$. This is consistent with the expectation that the high-flux sample selects preferentially for the most luminous sources, and these sources lie in the most highly biased environments (e.g. Mo & White 1996; Raccanelli et al. 2012).

We investigate whether the data provide information about the (largely unknown) high-redshift bias of radio-loud AGN. Here we fix the bias to the fiducial model at redshifts $z < 1.5$ and to a redshift-independent value above this. We constrain the high-redshift bias to be $b(z > 1.5) = 4.1 \pm 1.7$. The detection significance is reduced relative to the full sample because only high-redshift sources (≈1/3 of the total) constrain this parameter. The increase in bias between low- and high-redshift samples is consistent with the result of Lindsay et al. (2014b), who show that the bias $b(z)$ continues to increase above redshift $z = 2$, although we note that the significance is low.

We divide the source sample into those that have redshift estimates or not. A fraction of 0.27 of the FIRST sources have a reliable optical match as described in Section 2.2. The redshift distribution of these sources is strongly weighted to low redshifts, peaking around $z = 0.5$. Following Lindsay et al. (2014b) we can estimate the redshift distribution of the remaining sources by comparison with the SKADS simulated radio catalogue used to construct the model redshift distribution for the full sample. We construct independent overdensity maps for these two radio populations (with/without redshift) and recompute the data cross-spectra. We also recalculate the theoretical cross-correlation curves, accounting for the different source distributions, as a function of a redshift-independent bias term b. We find $b = 2.1 \pm 1.1$ at an effective redshift $z_{\rm eff} = 0.5$ for the sample with redshifts, and $b = 3.1 \pm 0.8$ at an effective redshift $z_{\rm eff} = 1.6$ for the sample without redshifts, shown in Fig. 9. Although not formally significantly different, this is consistent with an increasing bias as a function of redshift.

3.2 Comparison to previous bias measurements

Geach et al. (2013) find a constant linear bias $b = 1.61 \pm 0.22$ at an effective redshift $z \approx 1$ for IR-selected quasars from *WISE* in cross-correlation with the SPT convergence map. At the same effective redshift, our bias amplitude determination corresponds to $b(z = 1) = 2.6 \pm 0.6$. Their quasar sample is shallower (42 sources deg^{-2}) than in the FIRST maps presented here (71 sources deg^{-2}), and the predominant signal comes from $z < 2$ sources (there are expected to be no $z > 3$ sources). The higher bias determination presented here is consistent with a more highly biased population of sources being sampled.

Sherwin et al. (2012) constrain a constant linear bias $b = 2.5 \pm 0.6$ for optically selected quasars from SDSS totalling 75 sources deg^{-2}.

Downloaded from http://mnras.oxfordjournals.org/ at NASA Goddard Space Flight Ctr on November 16, 2015

The redshift distribution of these sources peaks at $z = 1.4$. White et al. (2012) determine $b = 3.8 \pm 0.3$ from the two-point correlation function of quasars in the Baryon Oscillation Spectroscopic Survey across the redshift range $2.2 < z < 2.8$. Comparing with Fig. 9, this is in good agreement with our result and assumed bias model.

Lindsay et al. (2014a) measure the bias as a function of redshift by auto-correlation of radio sources from the GAMA survey to the same depth (1 mJy) as this analysis. Assuming comoving clustering, their low-redshift measurement, $b(z \approx 0.5) = 2.13^{+0.90}_{-0.76}$, is consistent with the results presented here, while at high redshift they find $b(z \approx 1.5) = 9.45^{+0.58}_{-0.67}$, significantly higher than seen in this analysis. However, we note that there is no cosmic variance contribution included in their quoted uncertainties, and that they show that this is a large effect for the small GAMA fields for sources at lower redshift. We suggest that the high value of their measurement relative to that presented here is consistent with cosmic variance.

Our result probes the multipole range $100 < l < 3000$, corresponding to physical scales $\approx$ 2–60 Mpc at the effective redshift $z_{\rm eff} = 1.5$. As seen in Fig. 5, low- and high-redshift sources contribute to the cross-spectrum differently as a function of scale. At the scales probed by the Planck Collaboration XVII (2014b) lensing cross-correlation analysis with NVSS radio sources ($l < 400$), $z > 1.5$ sources contribute $\sim$1/3 of the total cross-spectrum, whereas at smaller scales these sources contribute equally alongside the $z < 1.5$ sources. By measuring the cross-spectrum across a wide range of scales, one might distinguish between low- and high-redshift sources. Future high-precision determinations of this cross-spectrum will go further in breaking the degeneracy between source populations and constraining the bias as a function of redshift.

We can translate the constraint on the AGN bias at redshift $z_{\rm eff} = 1.5$ into an inference on the mass of the halo in which the typical AGN source resides. Using the fitting function of Tinker et al. (2010), we find $\log(M_{\rm halo}/{\rm M}_\odot) = 13.6^{+0.3}_{-0.4}$, assuming that haloes virialize at a density ratio $\Delta = 200$ times that of the Universe at the epoch of formation. If we instead adopt the Mo & White (1996) prescription relating bias to halo mass, as used in this analysis and Wilman et al. (2008) to construct the bias models for each radio population, we find a consistent figure of $\log(M_{\rm halo}/{\rm M}_\odot) = 13.5^{+0.3}_{-0.4}$. This observed mass is higher than that seen in e.g. Sherwin et al. (2012): $\log(M_{\rm halo}/{\rm M}_\odot) = 12.9^{+0.3}_{-0.5}$ and Geach et al. (2013): $\log(M_{\rm halo}/(h^{-1}\,{\rm M}_\odot)) = 12.3^{+0.3}_{-0.2}$. This is consistent with the observations of e.g. Shen et al. (2009) and Hatch et al. (2014) that the environments of radio-loud AGN are significantly denser than those for radio-quiet AGN.

We find a high bias for these sources compared to optically and IR-selected AGN. This analysis provides complementary information by probing the bias of radio-selected AGN which, in the context of previous work, is indicative of bias evolution and a very large halo mass for these sources. The broad picture is that of an increasing bias as a function of redshift, and of radio-loud AGN occupying more massive haloes than radio-quiet AGN across a similar redshift range.

Our findings are in line with studies of the stellar masses (e.g. Jarvis et al. 2001b; Seymour et al. 2007) and environments (e.g. Wylezalek et al. 2013; Hatch et al. 2014) of powerful radio sources to high redshift. Specifically, we find strong evidence that powerful radio sources are more highly biased tracers of the dark matter density field than other AGN that are detectable to high redshift (e.g. quasars; Sherwin et al. 2012; Geach et al. 2013). As well as being important for tracing the underlying dark matter distribution with techniques such as those described in Ferramacho et al. (2014), this also suggests that mechanical feedback from the jets of *powerful* radio AGN should only have a significant effect on the level of star formation within the most massive dark matter haloes at all epochs. However, we note that such an effect can not only have an impact on both the AGN host galaxy (e.g. Bower et al. 2006; Croton et al. 2006; Hopkins et al. 2006; Dubois et al. 2013; Mocz, Fabian & Blundell 2013), but also the wider cluster environment (e.g. Rawlings & Jarvis 2004).

3.3 Modelling limitations and astrophysical systematics

Because $C_l^{\kappa g}$ depends only on the product $b(z){\rm d}n/{\rm d}z$, and we constrain only its normalization, we stress that the results presented here are contingent on the assumed redshift evolution of the bias and redshift distribution of the sources.

The SKADS simulation is populated using empirical radio luminosity functions as described in Wilman et al. (2008). Extrapolation of the empirical luminosity functions into unobserved regimes will lead to inaccuracies in the inferred redshift distribution and bias model. To investigate the sensitivity of our measurement to uncertainties about the source redshift distribution, we recompute the theoretical spectra, unrealistically removing all sources above redshift $z > 3$ when calculating ${\rm d}n/{\rm d}z$; at high redshift the underlying ${\rm d}n/{\rm d}z$ is most uncertain and likely depends on radio luminosity (e.g. Jarvis & Rawlings 2000; Jarvis et al. 2001b; Wall et al. 2005; Rigby et al. 2011). Fitting the theoretical cross-spectrum as in Section 3, we find $b(z_{\rm eff} = 1.2) = 3.2 \pm 0.8$, representing a $\sim 0.25\sigma$ shift from the primary result under this significant perturbation of the theoretical redshift distribution. We thus do not expect that the source distribution uncertainty strongly biases our result, although future analyses with higher statistical power will require careful consideration of this systematic uncertainty.

We fix the cosmology to the *Planck* best-fitting values throughout this analysis, which could affect the inference of the AGN bias. However, the significant (40σ) detection of the *Planck* lensing auto-spectrum means that model uncertainty from the cosmology is sub-dominant with respect to astrophysical uncertainties (Planck Collaboration XV 2015). Perturbing the *Planck* best-fitting cosmological parameters by $+1\sigma$ and recomputing the theoretical cross-spectrum, $C_l^{\kappa g}$, the amplitude is shifted by <6 per cent across all relevant scales; we thus neglect this source of systematic uncertainty.

Potential astrophysical systematic contaminants include infrared sources, Sunyaev–Zeldovich clusters and Galactic cirrus. Sherwin et al. (2012) show that these constitute small effects on the measured cross-spectrum between quasars and lensing (<10 per cent in total), negligible at the level of statistical uncertainty in this analysis. Although the sources studied in Sherwin et al. (2012) are optically selected AGN, we expect the result to hold for the radio-loud AGN of this analysis given the roughly similar redshift distributions. Furthermore, bright radio sources ($\gtrsim$ 5 mJy) in the CMB temperature and polarization maps are subtracted prior to lensing reconstruction, using a match-filtered source template map, thus mitigating radio-source contamination in the CMB convergence map (Das et al. 2011; van Engelen et al. 2014).

4 CONCLUSIONS

We present a measurement of the angular cross-power spectrum between lensing convergence from ACT and the overdensity of radio sources identified in the FIRST survey, rejecting the null hypothesis of no correlation at 4.4σ significance. The data are well fitted

Downloaded from http://mnras.oxfordjournals.org/ at NASA Goddard Space Flight Ctr on November 16, 2015

by the *Planck* best-fitting Λ cold dark matter (ΛCDM) cosmological model where we model the source population with a redshift-dependent bias. We interpret the result in terms of a constraint on the bias of AGN, which dominate the FIRST sample, considering various bias models and data splits to probe different redshift regimes and AGN populations, and put these in the context of previous measurements of AGN bias. We translate the bias determination into a constraint on the mass of the host haloes, corroborating previous work showing that the environments of radio-loud AGN are more dense than those of optically selected AGN.

We consider various sources of systematic uncertainty, both astrophysical contaminants and modelling limitations. We conclude that our results are robust to these effects. As deeper and wider radio surveys and improved lensing maps become available, these systematic effects will become increasingly important to measure and model accurately. The auto- and cross-spectra $\{C_l^{gg}, C_l^{\kappa\kappa}, C_l^{\kappa g}\}$ provide complementary information about the large-scale structure they probe, with the cross-spectrum in particular being robust to systematic biases particular to each data set. A full analysis will simultaneously estimate the three power spectra, marginalizing over uncertainty in the redshift distribution and cosmology (Pearson & Zahn 2014). With current data there are strong degeneracies in the cross-spectrum amplitude between sources from different redshifts. The shape of the power spectra contains information about the bias evolution, and larger, more sensitive surveys will allow us to break these degeneracies.

The measurement of the high bias (and correspondingly large halo mass) of this radio population, relative to other dark matter tracers, indicates that these sources would be useful in the multi-tracer technique of Ferramacho et al. (2014). Using all the information in auto- and cross-correlations between multiple tracers, which differentially trace the dark matter, will provide tight constraints on primordial non-Gaussianity by reducing the impact of cosmic variance at large scales.

The SKA will serve as a deep probe of large-scale structure in the Universe, it will be limited by different systematics than optical surveys and the observed source distribution will be skewed to higher redshifts than either LSST or *Euclid* (Laureijs et al. 2011; Amendola et al. 2013; Jarvis et al. 2015). Kirk et al. (2015) show that next-generation CMB lensing experiments, in combination with the SKA, will constrain the amplitude of the lensing-radio density cross-spectrum to the sub-per cent level. With tight constraints on cosmology, this translates into <1 per cent uncertainty on the bias amplitude, offering broad scope for probing the history and evolution of AGN. Future high-precision measurements of $C_l^{\kappa g}$ will use information about the shape of the cross-spectrum, and source tomography, to constrain the bias as a function of redshift, calibrating galaxy redshift surveys and constraining extensions to ΛCDM.

The cross-correlation of CMB lensing with tracers of large-scale structure will become an increasingly important calibrator for future high-precision galaxy and weak-lensing surveys.

ACKNOWLEDGEMENTS

RA is supported by an STFC PhD studentship. This work was supported by the US National Science Foundation through awards AST-0408698 and AST-0965625 for the ACT project, as well as awards PHY-0855887 and PHY-1214379. Funding was also provided by Princeton University, the University of Pennsylvania, Cornell University and a Canada Foundation for Innovation (CFI) award to UBC. ACT operates in the Parque Astronómico Atacama in Northern Chile under the auspices of the Comisión Nacional de Investigación Científica y Tecnológica de Chile (CONICYT). Computations were performed on the GPC supercomputer at the SciNet HPC Consortium. SciNet is funded by the CFI under the auspices of Compute Canada, the Government of Ontario, the Ontario Research Fund ï¿½ Research Excellence and the University of Toronto. The development of multichroic detectors and lenses was supported by NASA grants NNX13AE56G and NNX14AB58G. Funding from ERC grant 259505 supports SN, JD and TL. RD was supported by CONICYT grants QUIMAL-120001 and FONDECYT-1141113. We gratefully acknowledge support from the Misrahi and Wilkinson research funds.

REFERENCES

Abdalla F. B. et al., 2015, preprint (arXiv:1501.04035)
Ade P. A. R. et al. (POLARBEAR Collaboration), 2014, Phys. Rev. Lett., 113, 021301
Amendola L. et al., 2013, Living Rev. Relativ., 16, 6
Becker R. H., White R. L., Helfand D. J., 1995, ApJ, 450, 559
Bianchini F. et al., 2015, ApJ, 802, 64
Blake C., Wall J., 2002, MNRAS, 329, L37
Blake C. A., Abdalla F. B., Bridle S. L., Rawlings S., 2004a, New Astron. Rev., 48, 1063
Blake C., Mauch T., Sadler E. M., 2004b, MNRAS, 347, 787
Bleem L. E. et al., 2012, ApJ, 753, L9
Bock D. C.-J., Large M. I., Sadler E. M., 1999, AJ, 117, 1578
Bower R. G., Benson A. J., Malbon R., Helly J. C., Frenk C. S., Baugh C. M., Cole S., Lacey C. G., 2006, MNRAS, 370, 645
Camera S., Santos M. G., Bacon D. J., Jarvis M. J., McAlpine K., Norris R. P., Raccanelli A., Röttgering H., 2012, MNRAS, 427, 2079
Carilli C. L., Rawlings S., 2004, New Astron. Rev., 48, 979
Condon J. J., Cotton W. D., Greisen E. W., Yin Q. F., Perley R. A., Taylor G. B., Broderick J. J., 1998, AJ, 115, 1693
Condon J. J., Cotton W. D., Broderick J. J., 2002, AJ, 124, 675
Cress C. M., Helfand D. J., Becker R. H., Gregg M. D., White R. L., 1996, ApJ, 473, 7
Croton D. J. et al., 2006, MNRAS, 365, 11
Das S. et al., 2011, Phys. Rev. Lett., 107, 021301
Das S. et al., 2014, J. Cosmol. Astropart. Phys., 4, 014
de Zotti G., Massardi M., Negrello M., Wall J., 2010, A&AR, 18, 1
Dubois Y., Gavazzi R., Peirani S., Silk J., 2013, MNRAS, 433, 3297
Feng C., Aslanyan G., Manohar A. V., Keating B., Paar H. P., Zahn O., 2012, Phys. Rev. D, 86, 063519
Fernandes C. A. C. et al., 2015, MNRAS, 447, 1184
Ferramacho L. D., Santos M. G., Jarvis M. J., Camera S., 2014, MNRAS, 442, 2511
Fornengo N., Perotto L., Regis M., Camera S., 2015, ApJL, 802, L1
Geach J. E. et al., 2013, ApJ, 776, L41
Hand N. et al., 2015, Phys. Rev. D, 91, 062001
Hatch N. A. et al., 2014, MNRAS, 445, 280
Helfand D. J., White R. L., Becker R. H., 2015, ApJ, 801, 26
Hirata C. M., Ho S., Padmanabhan N., Seljak U., Bahcall N. A., 2008, Phys. Rev. D, 78, 043520
Hopkins P. F., Somerville R. S., Hernquist L., Cox T. J., Robertson B., Li Y., 2006, ApJ, 652, 864
Hu W., Okamoto T., 2002, ApJ, 574, 566
Jarvis M. J., Rawlings S., 2000, MNRAS, 319, 121
Jarvis M. J., Rawlings S., 2004, New Astron. Rev., 48, 1173
Jarvis M. J., Rawlings S., Eales S., Blundell K. M., Bunker A. J., Croft S., McLure R. J., Willott C. J., 2001a, MNRAS, 326, 1585
Jarvis M. J., Rawlings S., Willott C. J., Blundell K. M., Eales S., Lacy M., 2001b, MNRAS, 327, 907
Jarvis M. J. et al., 2013, MNRAS, 428, 1281
Jarvis M. J., Bacon D., Blake C., Brown M. L., Lindsay S. N., Raccanelli A., Santos M., Schwarz D., 2015, preprint (arXiv:1501.03825)

Downloaded from http://mnras.oxfordjournals.org/ at NASA Goddard Space Flight Ctr on November 16, 2015

Kamionkowski M., Kosowsky A., Stebbins A., 1997, Phys. Rev. D, 55, 7368
Kirk D., Benoit-Lévy A., Abdalla F. B., Bull P., Joachimi B., 2015, preprint (arXiv:1501.03848)
Knox L., 1995, Phys. Rev. D, 52, 4307
Laureijs R. et al., 2011, preprint (arXiv:1110.3193)
Lewis A., Challinor A., Lasenby A., 2000, ApJ, 538, 473
Lindsay S. N. et al., 2014a, MNRAS, 440, 1527
Lindsay S. N., Jarvis M. J., McAlpine K., 2014b, MNRAS, 440, 2322
Maartens R., Zhao G.-B., Bacon D., Koyama K., Raccanelli A., 2013, J. Cosmol. Astropart. Phys., 2, 44
Maartens R., Abdalla F. B., Jarvis M., Santos M. G., for the SKA Cosmology SWG 2015, preprint (arXiv:1501.04076)
Madhavacheril M. et al., 2015, Phys. Rev. Lett., 114, 151302
Magliocchetti M., Maddox S. J., Lahav O., Wall J. V., 1998, MNRAS, 300, 257
Mauch T., Sadler E. M., 2007, MNRAS, 375, 931
Mo H. J., White S. D. M., 1996, MNRAS, 282, 347
Mocz P., Fabian A. C., Blundell K. M., 2013, MNRAS, 432, 3381
Naess S. et al., 2014, J. Cosmol. Astropart. Phys., 10, 7
Niemack M. D. et al., 2010, Proc. SPIE, 7741, 77411S
Norris R. P. et al., 2013, PASA, 30, 20
Overzier R. A., Röttgering H. J. A., Rengelink R. B., Wilman R. J., 2003, A&A, 405, 53
Pearson R., Zahn O., 2014, Phys. Rev. D, 89, 043516
Planck Collaboration XVI, 2014a, A&A, 571, A16
Planck Collaboration XVII, 2014b, A&A, 571, A17
Planck Collaboration XVIII, 2014c, A&A, 571, A18
Planck Collaboration XV, 2015, preprint (arXiv:1502.01591)
Raccanelli A. et al., 2012, MNRAS, 424, 801
Rawlings S., Jarvis M. J., 2004, MNRAS, 355, L9
Rengelink R. B., Tang Y., de Bruyn A. G., Miley G. K., Bremer M. N., Roettgering H. J. A., Bremer M. A. R., 1997, A&AS, 124, 259
Rigby E. E., Best P. N., Brookes M. H., Peacock J. A., Dunlop J. S., Röttgering H. J. A., Wall J. V., Ker L., 2011, MNRAS, 416, 1900
Rocca-Volmerange B., Le Borgne D., De Breuck C., Fioc M., Moy E., 2004, A&A, 415, 931
Santos M. G. et al., 2015, preprint (arXiv:1501.03989)
Seljak U., Warren M. S., 2004, MNRAS, 355, 129
Seymour N. et al., 2007, ApJS, 171, 353
Shen Y. et al., 2009, ApJ, 697, 1656
Sherwin B. D. et al., 2012, Phys. Rev. D, 86, 083006
Smith R. E. et al., 2003, MNRAS, 341, 1311
Smith K. M., Zahn O., Doré O., 2007, Phys. Rev. D, 76, 043510
Story K. T. et al., 2014, preprint (arXiv:1412.4760)
Takahashi R., Sato M., Nishimichi T., Taruya A., Oguri M., 2012, ApJ, 761, 152
Tinker J. L., Robertson B. E., Kravtsov A. V., Klypin A., Warren M. S., Yepes G., Gottlöber S., 2010, ApJ, 724, 878
van Engelen A. et al., 2014, preprint (arXiv:1412.0626)
Wall J. V., Jackson C. A., Shaver P. A., Hook I. M., Kellermann K. I., 2005, A&A, 434, 133
White R. L., Becker R. H., Helfand D. J., Gregg M. D., 1997, ApJ, 475, 479
White M. et al., 2012, MNRAS, 424, 933
Wilman R. J. et al., 2008, MNRAS, 388, 1335
Wilman R. J., Jarvis M. J., Mauch T., Rawlings S., Hickey S., 2010, MNRAS, 405, 447
Wylezalek D. et al., 2013, ApJ, 769, 79
York D. G. et al., 2000, AJ, 120, 1579

This paper has been typeset from a TEX/LATEX file prepared by the author.

Downloaded from http://mnras.oxfordjournals.org/ at NASA Goddard Space Flight Ctr on November 16, 2015